

(Fig. 3B) and $-y$ (Fig. 3C) directions. All three experiments were performed with pristine films. The upper panels show the sum ΣI of two adjacent intensity maxima as shown in Fig. 2. The angle of incidence of the fundamental beam was chosen such that the Fresnel factors are higher at the lens-prism interface compared with the prism-air interface (6). Thus, the area of increased SHG intensity directly reflects the size of the contact area. The middle panels show maps of ΔI . For normal loading of the lens (Fig. 3A), ΔI changes sign across the contact area, indicating that the forces are axially symmetric with respect to the initial point of contact, causing a radial alignment of the molecules. Because we only probed alignment along the y axis, $|\Delta I|$ for molecules aligned along the x axis is zero and gradually increases with increasing alignment along y . This is seen in the radially symmetric case in which ΔI changes sign at $y = 0$. In contrast, rolling causes a unidirectional alignment over the whole contact area (Fig. 3, B and C).

It is evident from the alignment seen under both normal loading and rolling conditions that shear forces act on the film. However, their origin is not clear at present. Microslip due to the difference in the elastic constants of the prism and the lens seems to be too small to account for the alignment, and, furthermore, an alignment pattern different from those depicted in Fig. 3, B and C, is expected from standard models in contact mechanics (23). Thus, other mechanisms should be considered, such as squeezing of the organic film, which would produce a lateral force originating from the point of highest pressure outward. Also, interfacial contaminations such as an adsorbed water film that is squeezed out of the contact area under loading could give rise to an additional shear force.

The results presented here demonstrate that the tribological properties of surface coatings and lubricants between two bodies can be monitored in situ to study molecular changes as a function of loading conditions and to monitor their durability or wear. They can be extended to sum frequency generation (SFG) (28) studies, which will then allow the study of confined organic films more relevant to technical applications than the model system presented here.

References and Notes

1. B. Bhushan, J. N. Israelachvili, U. Landman, *Nature* **374**, 607 (1995).
2. R. Maboudian, *MRS Bull.* (June 1998), p. 47.
3. J. A. Harrison and S. S. Perry, *MRS Bull.* (June 1998), p. 27.
4. S. A. Joyce, R. C. Thomas, J. E. Houston, T. A. Michalske, R. M. Crooks, *Phys. Rev. Lett.* **68**, 2790 (1992).
5. Q. Du *et al.*, *Phys. Rev. B* **51**, 7456 (1995).
6. R. Frankel, G. E. Butterworth, C. D. Bain, *J. Am. Chem. Soc.* **120**, 203 (1998).
7. A. Berman, S. Steinberg, S. Campbell, A. Ulman, J. Israelachvili, *Tribol. Lett.* **4**, 43 (1998).
8. J. N. Israelachvili and D. Tabor, *Nature* **241**, 148 (1973).

9. J. N. Israelachvili, *J. Vac. Sci. Technol. A* **10**, 2961 (1992).
10. G. Liu and M. Salmeron, *Langmuir* **10**, 367 (1994).
11. S. Karaborni, *Phys. Rev. Lett.* **73**, 1668 (1994).
12. K. J. Tupper and D. Brenner, *Langmuir* **10**, 2335 (1994).
13. K. J. Tupper, R. J. Colton, D. W. Brenner, *Langmuir* **10**, 2041 (1994).
14. R. Henda, M. Grunze, A. J. Pertsin, *Tribol. Lett.* **5**, 191 (1998).
15. J. I. Siepmann and I. R. McDonald, *Langmuir* **9**, 2351 (1993).
16. S. H. J. Idziak *et al.*, *Science* **264**, 1915 (1994).
17. P. M. Cann and H. A. Spikes, *Tribol. Trans.* **34**, 248 (1991).
18. G. J. Johnston, R. Wayte, H. A. Spikes, *Tribol. Trans.* **34**, 187 (1991).
19. Y. R. Shen, *The Principles of Nonlinear Optics* (Wiley, New York, 1984).
20. R. M. Corn and D. A. Higgins, *Chem. Rev.* **94**, 107 (1994).
21. The sample preparation followed (29) with the use of a solution of *N*-[3-(trimethoxysilyl)propyl] 2,4-dinitrophenylamine in toluene.
22. D. S. Chemla and J. Zyss, Eds., *Nonlinear Optical Properties of Organic Molecules and Crystals*, vol. 1 (Academic Press, Orlando, FL, 1987).

23. K. L. Johnson, *Contact Mechanics* (Cambridge Univ. Press, Cambridge, 1985).
24. The following data were used in the calculation. The radius of the curvature of the lens was 250 mm. Elastic moduli of the SF10 glass prism and the BK7 glass lens were 64 GN/m² and 82 GN/m², respectively. The Poisson ratios were 0.23 for SF10 and 0.206 for BK7.
25. B. U. Felderhof, A. Bratz, G. Marovsky, O. Roders, F. Sieverdes, *J. Opt. Soc. Am. B* **10**, 1824 (1993).
26. Because a detailed treatment is beyond the scope of this report, we make the simplifying assumption that the signal originates only from the organic layer. This does not hold exactly (27) but can be neglected for the purpose of this report.
27. A. Legant, thesis, University of Heidelberg, Heidelberg, Germany (1999).
28. C. D. Bain, in *Modern Characterization Methods of Surfactant Systems*, B. P. Binks, Ed. (Dekker, New York, 1999), pp. 336–373.
29. K. Bierbaum *et al.*, *Langmuir* **11**, 512 (1995).
30. This work was funded by the Office of Naval Research. Additional support from the Deutsche Forschungsgemeinschaft and the Fond der Chemischen Industrie is gratefully acknowledged. We are grateful to W. Eck for purifying the DNS.

1 September 1999; accepted 22 November 1999

Ultrafast Mid-Infrared Response of YBa₂Cu₃O_{7-δ}

R. A. Kaindl,¹ M. Woerner,¹ T. Elsaesser,^{1*} D. C. Smith,² J. F. Ryan,² G. A. Farnan,³ M. P. McCurry,³ D. G. Walmsley³

Optical spectra of high-transition-temperature superconductors in the mid-infrared display a gap of in-plane conductivity whose role for superconductivity remains unresolved. Femtosecond measurements of the mid-infrared reflectivity of YBa₂Cu₃O_{7-δ} after nonequilibrium optical excitation are used to demonstrate the ultrafast fill-in of this gap and reveal two gap constituents: a picosecond recovery of the superconducting condensate in underdoped and optimally doped material and, in underdoped YBa₂Cu₃O_{7-δ}, an additional sub-picosecond component related to pseudogap correlations. The temperature-dependent amplitudes of both contributions correlate with the antiferromagnetic 41-millielectronvolt peak in neutron scattering, supporting the coupling between charges and spin excitations.

A number of energy-sensitive studies on high-transition-temperature (high T_C) cuprate superconductors including tunneling (1), angular-resolved photoemission (2), neutron scattering (3), Raman scattering (4), and infrared reflectivity (5–8) suggest that understanding the elementary excitations in the mid-infrared energy range ($\hbar\omega \approx 40$ to 200 meV) in the vicinity of the superconducting gap is essential for clarifying the mechanisms behind formation of the superconducting condensate. In particular, the low-energy electromagnetic response of such cuprates contains valuable information on electronic excitations and their correlated dynamics.

¹Max-Born-Institut für Nichtlineare Optik und Kurzzeitspektroskopie, D-12489 Berlin, Germany. ²Department of Physics, Clarendon Laboratory, Oxford University, Oxford OX1 3PU, UK. ³Department of Pure and Applied Physics, Queen's University of Belfast, Belfast BT7 1NN, UK.

*To whom correspondence should be addressed.

When temperature T is lowered below the superconducting transition in optimally doped materials, the most pronounced changes of the reflectivity $R(\omega, T)$ for light of frequency ω polarized parallel to the superconducting CuO₂ planes [(*ab*)-plane reflectivity] appear in the spectral range around $\hbar\omega \approx 100$ meV. These reflectivity changes (Fig. 1A) are directly connected with a strong depression of the in-plane conductivity (Fig. 1C), which has been attributed to the opening of a gap for electronic transitions involving inelastic collisions. A straightforward association with the superconducting gap, however, is hampered by the observation that, in underdoped cuprates, such features already occur at temperatures T^* substantially higher than T_C (Fig. 1, B and D) and are termed pseudogap (5–8).

While stationary infrared spectroscopy measures the total of all contributions to the mid-infrared reflectivity and cannot clearly discern spectrally similar components in the pseudogap

regime, nonlinear time-resolved spectroscopy could provide such a distinction by separating the components in the time domain. Previous ultrafast optical experiments with high- T_C superconductors have given information on the time scales of carrier and condensate relaxation dynamics by nonequilibrium excitation of the carrier system at photon energies of 1.5 eV and subsequently studying its dynamics either at the same interband energies (9–11) or in the far-infrared around $\hbar\omega \approx 0$ to 3 meV (12). Here, we present experimental results probing the mid-infrared spectra in high- T_C superconductors on ultrafast time scales.

The superconductor is excited by 20-fs (pump) pulses at 1.6 eV from a mode-locked, cavity-dumped Ti:sapphire laser operating at a 2-MHz repetition rate. Mid-infrared (probe) pulses broadly tunable from 60 to 180 meV are derived from a newly developed difference frequency mixing scheme, with pulse durations typically of 150 fs (13). We present results for optimally doped ($T_C = 88 \pm 0.7$ K) and underdoped ($T_C = 68 \pm 1.5$ K) thin films of YBaCu₃O_{7- δ} (YBCO). We achieved underdoping (deoxygenation) by sintering optimally doped films at reduced oxygen pressure (14, 15). The 200-nm-thick twinned films are *c*-axis oriented; thus the mid-infrared beam, polarized parallel to the sample surface, probes directly the (*ab*)-plane reflectivity. The change of the reflected mid-infrared intensity induced by the pump pulse is recorded as a function of delay and spectral position E_{probe} of the probe pulses (16).

In the time-resolved mid-infrared response of optimally doped YBCO at $E_{\text{probe}} = 90$ meV (Fig. 2A), a fast, subpicosecond reflectivity increase to $\Delta R/R_0 \approx 3 \times 10^{-3}$ is followed by a decay on a much longer time scale of about 5 ps. With increasing sample temperature, the amplitude of $\Delta R/R_0$ decreases and, around T_C , changes its sign accompanied by a relaxation speedup. This distinction between reflectivity changes at temperatures $T < T_C$ and $T > T_C$ is confirmed by the transient spectra of $\Delta R/R_0$ (Fig. 2, C and D). Below T_C (Fig. 2C) ($T = 14$ K), the spectra peak sharply at $E_{\text{probe}} = 90$ meV. The energy position of this peak and the zero crossing at 70 meV remains constant for all delay times. The same holds true for other temperatures below T_C . Above T_C (Fig. 2D) ($T = 94$ K), the behavior drastically changes to a spectrally flat response.

We now compare the time-resolved reflectivity spectra to the changes induced in the stationary (*ab*)-plane reflectivity $R(\omega, T)$ as the sample temperature is raised from below to above T_C . In Fig. 1 (A and C), the difference of reflectivity spectra of our samples above T_C (95 K) and below T_C (20 K) is shown along with the normalized optical conductivity as obtained from Kramers-Kronig analysis. The optical conductivity, which is a measure of the oscillator strength, exhibits a broad depletion below about

100 meV, which occurs with the onset of superconductivity and corresponds to a peak in the difference reflectivity spectra around 100 meV. The shape of this peak closely matches our transient reflectivity spectra below T_C (Fig. 2C), which confirms that the ultrafast transients directly show the ultrafast fill-in and subsequent recovery of this mid-infrared conductivity gap.

Below T_C , the dynamics in the optimally doped sample is dominated by the slow relaxation of about 5 ps. Experiments probing the electrodynamic signature of the superconducting condensate in the far-infrared (12) have shown that absorption of near-infrared photons strongly reduces the condensate density (with a concurrent increase of Drude-like quasiparticle absorption), which re-forms on the same 5-ps time scale observed here. A comparison with such results is straightforward as the far-infrared response obeys basic electrodynamic properties generally valid for any superconducting condensate. Thus, the conductivity gap dynamics in the mid-infrared is directly determined by the depletion and re-formation of the superconducting condensate. With increasing

sample temperature, the initial density of the condensate, and thus the amplitude of the reflectivity change, decreases (Fig. 2B, solid squares) ($E_{\text{probe}} = 90$ meV).

Much faster dynamics and featureless spectra are found for the reflectivity changes above T_C (Fig. 2, A and D). This is attributed to cooling of a hot quasi-equilibrium electron gas, giving rise to reflectivity changes similar to those observed in metals (17).

A direct association of the conductivity gap found below T_C with the superconducting gap has been impeded by the fact that the stationary reflectivity of underdoped cuprates shows a similar conductivity decrease to occur already below the pseudogap temperature $T^* > T_C$ ($T^* \approx 160$ K in our underdoped sample) (5–8). Here, our femtosecond data provide a much clearer picture. Figure 3 shows time-resolved $\Delta R/R_0$ data for the underdoped sample at two different spectral positions of $E_{\text{probe}} = 90$ and 145 meV. The data taken below T_C (blue and black lines, lower panels) display an overall dynamics, which extend well into the picosecond regime and cannot be described by a sin-

Fig. 1. Stationary reflectivity and conductivity spectra of the samples studied in the femtosecond experiments. (A and B) Change $R(T_a) - R(T_b)$ of the stationary reflectivity $R(T)$ when temperature was raised from T_b to T_a for optimally doped [$T_C = 88$ K] (A) and underdoped [$T_C = 68$ K] (B) YBCO. (C and D) Real part of optical conductivity $\sigma_1(\omega, T)$ normalized to its value at $T = 200$ K as obtained from Kramers-Kronig analysis of the reflectivity spectra at various lattice temperatures for optimally doped (C) and underdoped (D) ($T_C = 68$ K) YBCO.

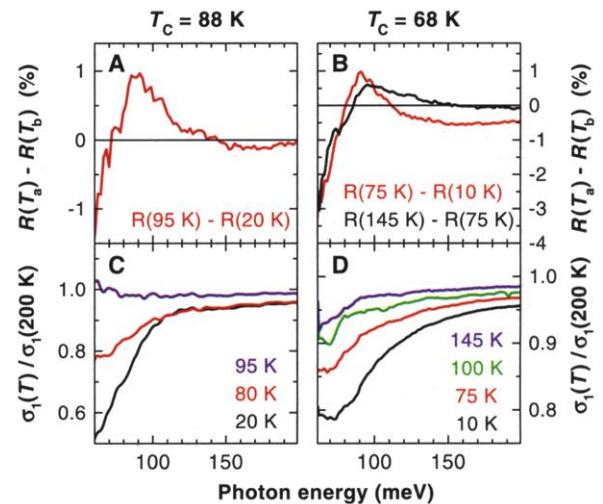


Fig. 2. Optimally doped YBCO. (A) Transient reflectivity change $\Delta R/R_0 = [R(t) - R_0]/R_0$ [$R(t)$ and R_0 are reflectivity with and without excitation, respectively] as a function of time delay between near-infrared pump and mid-infrared probe pulses (probe photon energy $E_{\text{probe}} = 90$ meV; T , sample temperature). (B) Solid squares, temperature dependence of $A_N(T) = A(T)/A(10 \text{ K})$, shown for data below T_C where $A(T) = \max(\Delta R/R_0)$ denotes maximum amplitude of transients at temperature T . Open circles, amplitude of the 41-meV resonance peak obtained from inelastic neutron scattering in (3) normalized to the 10 K value. (C and D) Transient differential reflectivity spectra at different time delays between pump and probe. Sample temperatures are $T = 14 \text{ K} \ll T_C$ (C) and $T = 94 \text{ K} > T_C$ (D).

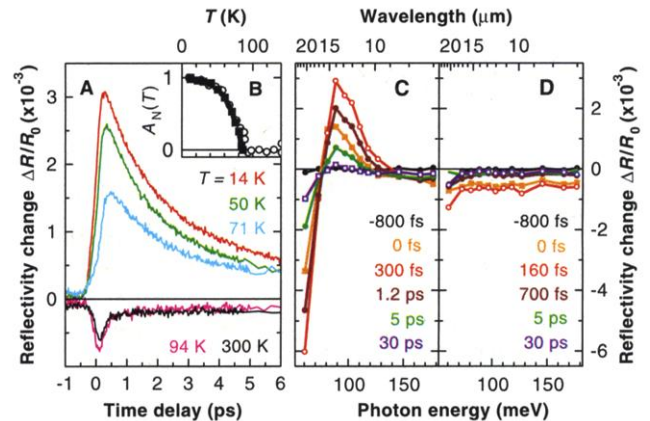
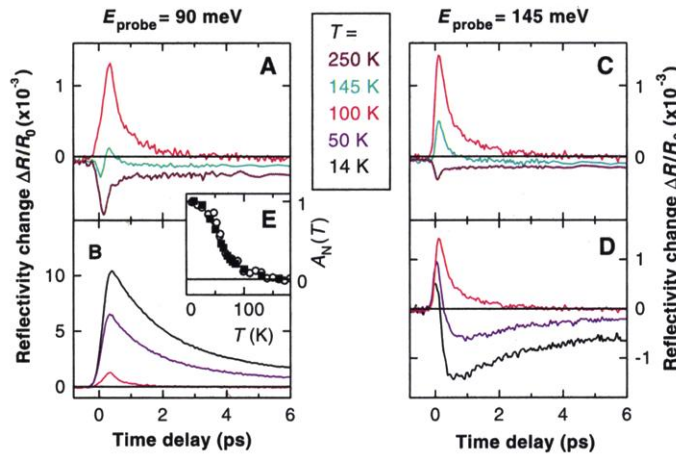


Fig. 3. Underdoped YBCO. Transient reflectivity changes $\Delta R(t)/R_0$ at $E_{\text{probe}} = 90$ meV (A and B) and $E_{\text{probe}} = 145$ meV (C and D) for different sample temperatures. (E) Temperature dependence of the normalized amplitude $A_N(T)$ (solid squares) defined as in Fig. 2B compared with amplitude of the 41-meV resonance peak (open circles) of a $T_C = 63$ K underdoped YBCO sample, from (3).



gle—for example, exponentially decaying—component. Above T_C , the transients are dominated by a fast component at early delay.

We analyzed the data of Fig. 3 and results for other probe frequencies by singular value decomposition, a standard numerical procedure previously applied to, for example, analysis of transient femtosecond spectra in biomolecular spectroscopy (18). It finds the number of mutually independent—that is, uncorrelated—components in a given input matrix containing the experimental data, where rows and columns represent temporal and spectral positions, respectively. The resulting orthonormal basis set of functions is used to construct physically meaningful components by linear combination. As additional constraints, we have assumed that the (normalized) transients decay monotonically and that subpicosecond components have totally decayed for times longer than about 30 ps. The total signal is written $\Delta R(\omega, t) = \sum_i a_i(\omega) \times b_i(t)$, where $a_i(\omega)$ and $b_i(t)$ are spectrum and time evolution of the i th component. The results of this analysis are shown in Fig. 4. The $\Delta R/R_0$ transients are essentially described by two components, one with a slow decay (about 5 ps) and one with a much faster decay (about 700 fs). The slow component exhibits a decay dynamics (Fig. 4A) and a spectrum (Fig. 4B) almost identical with that of the condensate in the optimally doped sample. In particular, it disappears completely above T_C . The fast component (Fig. 4A, spectra in Fig. 4C) exists both below and above T_C up to $T^* \approx 160$ K where the reflectivity transients change their sign and the decay rate becomes even faster (Fig. 3, A and C, brown curves).

The existence of the two dynamic components in the underdoped sample results in a temperature dependence of the $\Delta R/R_0$ amplitudes that is different from the optimally doped sample. At $E_{\text{probe}} = 90$ meV, a large fraction of the optically induced reflectivity changes has faded out at T_C but a substantial part remains even for significantly higher temperatures (Fig. 3E, solid squares). The above decomposition shows that this results from separate contribu-

tions of fast and slow components (Fig. 4D, as determined from the singular value decomposition amplitudes at $E_{\text{probe}} = 90$ meV) (19).

The observation of two different reflectivity components on a femtosecond time scale allows us to draw a new picture of the mid-infrared response of underdoped cuprates. Ultrafast excitation of the electronic system leads to a breakup of both condensed pairs and a second type of correlated carriers. The decomposition in Fig. 4D gives the relative contribution of those two types of quasiparticles. The dominating slow (about 5 ps) component follows the gap related to condensed pairs and fades out at T_C as in optimally doped samples. In contrast, the fast (about 700 fs) component exists up to the pseudogap temperature T^* . It results from the breakup and re-formation of carrier correlations, which have been ascribed to preformed pairs (20) or antiferromagnetic couplings (21).

The electronic response probed at mid-infrared energies far below the plasma frequency ($\approx 15,000$ cm^{-1}) is determined by intraband processes ≤ 100 meV close to the Fermi energy, which are indirect transitions formed by a charge excitation plus a momentum-conserving boson. Recent theories of the stationary infrared properties of cuprates (22, 23) suggest that the coupling to 41-meV antiferromagnetic (AF) spin fluctuations, which were observed as a resonance peak in inelastic neutron scattering (3) and treated theoretically in (21, 24), represents the dominant process in momentum conservation. As a result, the conductivity gap does not occur simply at twice the superconducting gap $2\Delta_0$ ($\Delta_0 \approx 25$ meV in YBCO) but includes the energy of the AF spin fluctuation. This model is strongly supported by a comparison of our femtosecond data with the strength of the 41-meV AF resonance peak. The amplitude of this peak decreases with temperature, as shown in Figs. 2B and 3E (open circles). Our optical measurements show an identical behavior of the $\Delta R/R_0$ amplitudes. The fact that charge- and spin-related amplitudes are proportional gives independent support for a prominent role of AF

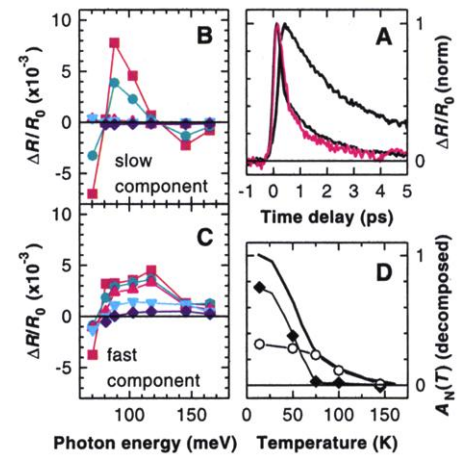


Fig. 4. Results of the singular value decomposition applied to the full data set for the underdoped sample, as explained in text. (A) Two components as normalized transients (black lines) obtained from decomposition at $T = 14$ K. Fast component retains its dynamics over temperature. For comparison, data at $T = 100$ K (magenta) are shown, where only the fast component exists. (B and C) Differential reflectivity spectra of the slow and fast transients at different temperatures: $T = 14$ K (red squares), 50 K (olive circles), 75 K (magenta up triangles), 100 K (cyan down triangles), 145 K (blue diamonds). (D) Amplitudes at $E_{\text{probe}} = 90$ meV of the fast (open circles) and slow (solid diamonds) components obtained from decomposition in (B) and (C) together with the total $A_N(T)$ (solid line) from Fig. 3E.

spin fluctuations in the mid-infrared absorption process.

A recent theoretical analysis of stationary infrared spectra has shown that coupling of quasiparticles to AF spin fluctuations is strong enough to support superconductivity up to $T_C = 100$ K (22), neglecting, however, the pseudogap behavior in underdoped materials. Our data give evidence that the mid-infrared response below T_C of both optimally and underdoped material is dominated by the superconducting condensate. This strongly suggests that indeed AF spin fluctuations play a prominent role for coupling in the superconducting condensate.

In summary, ultrafast nonlinear optical experiments allow us to separate the superconducting gap from the pseudogap contributions in the mid-infrared response of YBCO by monitoring their distinctly different dynamics.

References and Notes

- Ch. Renner, B. Revaz, J.-Y. Genoud, K. Kadowaki, *Ø. Fischer*, *Phys. Rev. Lett.* **80**, 14 (1998).
- Z. X. Shen and J. R. Schrieffer, *Phys. Rev. Lett.* **78**, 1771 (1997).
- P. Dai et al., *Science*, **284**, 1344 (1999).
- G. Blumberg, M. Kang, M. V. Klein, K. Kadowaki, C. Kendziora, *Science* **278**, 1427 (1997).
- J. Orenstein et al., *Phys. Rev. B* **42**, 6342 (1990).
- Z. Schlesinger et al., *Phys. C* **235-240**, 49 (1994).
- A. V. Puchkov, D. N. Basov, T. Timusk, *J. Phys. Condens. Matter* **8**, 10049 (1996).
- T. Timusk and B. Statt, *Rep. Prog. Phys.* **62**, 61 (1999).
- J. M. Chwalek et al., *Appl. Phys. Lett.* **57**, 1696 (1990).

10. S. G. Han, Z. V. Vardeny, K. S. Wong, O. G. Symko, G. Koren, *Phys. Rev. Lett.* **65**, 2708 (1990).
11. C. J. Stevens *et al.*, *Phys. Rev. Lett.* **78**, 2212 (1997) and references therein.
12. J. L. W. Siders, R. N. Jacobs, C. W. Siders, S. A. Trugman, S. A. Taylor, in *Ultrafast Phenomena XI*, T. Elsaesser *et al.*, Eds. (Springer, Berlin, 1998), pp. 365–367.
13. R. A. Kaindl, F. Eickemeyer, M. Woerner, T. Elsaesser, *Appl. Phys. Lett.* **75**, 1060 (1999).
14. H. F. Sakeek *et al.*, *J. Appl. Phys.* **70**, 2455 (1991).
15. G. A. Farnan, M. P. McCurry, D. G. Walmsley, unpublished data.
16. The excitation density in the experiments estimated from the average pump power (about 15 mW) and focus diameter (about 170 μm) was $1.5 \times 10^{19} \text{ cm}^{-3}$.
17. S. D. Brorson *et al.*, *Phys. Rev. Lett.* **64**, 2172 (1990).
18. S. Yamaguchi and H. Hamaguchi, *J. Mol. Struct.* **379**, 87 (1996).
19. This interpretation of the results is supported by measurements with different excitation intensities, showing a different saturation behavior of the two components.
20. V. J. Emery, S. A. Kivelson, O. Tzachar, *Phys. Rev. B* **56**, 6120 (1997).
21. D. Pines, *Z. Phys. B* **103**, 129 (1997).
22. J. P. Carbotte, E. Schachinger, D. N. Basov, *Nature* **401**, 354 (1999).
23. D. Munzar, C. Bernhard, M. Cardona, *Phys. C* **312**, 121 (1999).
24. E. Demler and S.-C. Zhang, *Nature* **396**, 733 (1998).
25. Supported by the European Union through the Training and Mobility of Researchers Ultrafast Network. We thank C. Stevens, P. Hamm, C. Lienau, G. A. Wagner, and J. E. Evetts for discussions and contributions to early stages of this work.

3 September 1999; accepted 23 November 1999

All-Optical Magnetic Resonance in Semiconductors

J. M. Kikkawa and D. D. Awschalom*

A scheme is proposed wherein nuclear magnetic resonance (NMR) can be induced and monitored using only optical fields. In analogy to radio-frequency fields used in traditional NMR, circularly polarized light creates electron spins in semiconductors whose hyperfine coupling could tip nuclear moments. Time-resolved Faraday rotation experiments were performed in which the frequency of electron Larmor precession was used as a magnetometer of local magnetic fields experienced by electrons in n-type gallium arsenide. Electron spin excitation by a periodic optical pulse train appears not only to prepare a hyperpolarized nuclear moment but also to destroy it resonantly at magnetic fields proportional to the pulse frequency. This resonant behavior is in many ways supportive of a simple model of optically induced NMR, but a curious discrepancy between one of the observed frequencies and classic NMR values suggests that this phenomenon is more complex.

Hyperfine interactions have been invaluable in probing solid-state systems. Optical pumping and detection of NMR (1–3) are sensitive measures of localized electronic states in semiconductors (4, 5), and have advanced our understanding of spin polarization in the quantum Hall regime (6). Instabilities of the electron-nuclear system that manifest in hysteresis of the electron magnetization have long been recognized (2, 7), and in quantum Hall systems this interplay has recently been found to be strong enough to dominate charge transport characteristics (8). Electron-nuclear coupling may also allow for the manipulation of coherent nuclear states in quantum computation (9). Here we propose that such interactions may enable the manipulation and detection of nuclear spin states with entirely optical methods, a scheme relevant to a broad variety of materials systems in which electron spins can be optically oriented and exhibit hyperfine coupling to nuclei.

We have performed a series of experiments that reveal magnetic resonance phenomena in gallium arsenide (GaAs) semiconductors occurring in the vicinity of nuclear frequencies and induced by an optical pulse train. Using optical detection of the electron Larmor frequency as a

sensitive magnetometer, we find that optical pumping induces local fields up to ~ 0.4 T in ~ 250 s, which is nine orders of magnitude slower than typical electronic time scales and is suggestive of nuclear polarization by conduction electrons. Furthermore, we propose that optical fields can resonantly tip nuclear moments, using periodically excited electron spin instead of conventional radio-frequency (RF) fields. Extending the technique of Larmor magnetometry, we discover a depolarization of local magnetic fields that is indeed resonant with the periodicity of optical excitation. One of the two observed resonances fields lies within measurement error of that predicted by our model for optical NMR, whereas the other differs by $\sim 11\%$ with the nearest isotope of the GaAs host. The latter finding is particularly surprising because the temperature and field dependence, time scale, linewidth, and optical saturation of the resonance amplitude are all consistent with our framework for NMR. Despite attempts to identify additional periodicities that might influence resonance, further study is necessary to clarify its underlying mechanism.

Time-resolved magneto-optical Faraday rotation, recently developed for measuring conduction band spin precession in semiconductors (10–13), is well suited for the study of nuclear moments in GaAs because the hyperfine interaction is particularly large in this semiconductor (2). Our pump-probe experiments use short

(~ 100 fs) time-delayed optical pulses tuned near the band-gap energy of the semiconductor and focused to a diameter of ~ 20 μm . A circularly polarized pump pulse, incident along the sample normal \hat{x} , excites an electronic magnetization, $\vec{S} \parallel \hat{x}$. An in-plane external field, $\vec{B} \parallel \hat{z}$, induces the subsequent Larmor precession of \vec{S} about \hat{z} . The projection of this spin motion along \hat{x} is recorded by the Faraday rotation, θ_F , of a linearly polarized, time-delayed probe pulse ($\theta_F \propto S_x$). As the pump-probe delay Δt is scanned, precession of $\vec{S}(\Delta t)$ causes S_x (and thus θ_F) to oscillate at the Larmor frequency $\omega_L = g_e \mu_B B_{\text{tot}} / \hbar$. Because the total magnetic field B_{tot} is the sum of the applied field and any additional local fields experienced by the electrons, Larmor frequency measurements can be used for magnetometry of hyperfine fields whenever the electron g factor, g_e , is known to be constant.

Electron spin precession for an n-type GaAs crystal with $n = 3 \times 10^{16} \text{ cm}^{-3}$ and a transverse field strength of $B = 5.19$ T is shown in Fig. 1A. The sample is held at temperature (T) = 5 K inside a magneto-optical cryostat containing a superconducting magnet. Details of sample preparation and measurement are given elsewhere (12). The pump's arrival at $\Delta t = 0$ initiates spin motion whose oscillatory frequency reflects a g factor of -0.44 and responds dynamically to changes in B_{tot} . The oscillation decay time T_2^* , despite a 100-fold decrease relative to data taken in zero field (12), exceeds the Larmor period by roughly two orders of magnitude and allows ω_L to be determined to high precision. Successive measures of ω_L can then be used to capture changes in B_{tot} over long time scales.

Because nuclear polarization can shift the electron spin resonance line (14), nuclear dynamics induced by optical pumping should be measurable in real-time measurements of the Larmor frequency. Instead of studying ω_L by capturing dozens of spin revolutions, as in Fig. 1A, we monitored a single revolution near the end of such a scan and used shifts in the Larmor angle, $\omega_L \Delta t$, to establish changes in ω_L at a fixed value of the applied field. This strategy improved temporal resolution, and by repeatedly sweeping Δt from 2660 to 2700 ps, the dynamics of $B_{\text{tot}} \propto \omega_L$ could be studied in 10-s intervals. The plot atop Fig. 1C shows the first scan, and subsequent scans are assembled in the

Department of Physics, University of California, Santa Barbara, CA 93106, USA.

*To whom correspondence should be addressed. E-mail: awsch@physics.ucsb.edu